Electrochemistry Communications 156 (2023) 107600

Contents lists available at ScienceDirect

Electrochemistry Communications

journal homepage: www.elsevier.com/locate/elecom

Boron-induced growth of highly textured Ag (1 1 1) films with nano-tentacle structures for the electrochemical reduction of CO_2 to CO

Kim Robert Gustavsen, Hao Huang, Erik Andrew Johannessen, Kaiying Wang *

Department of Microsystems, University of South-Eastern Norway, Horten 3184, Norway

ARTICLE INFO

Keywords:
AgB
Boron doped silver
Electrochemical CO_2 reduction
Nano-tentacles
Silver catalyst

ABSTRACT

Ag is a cost-effective alternative to Au as a catalyst for the electrochemical reduction of CO_2 into CO, but a reduction in the accompanying overpotential is required to make Ag viable. In this study we use B to modulate the catalytic performance of Ag towards the electrochemical reduction of CO_2 to CO. Initial DFT simulations discloses a deviation from the linear scaling relations with the inclusion of B that stabilizes the *COOH intermediate while weakening the binding strength of *CO. A magnetron co-sputtering process is used to develop a catalyst based on B-induced crystal growth of highly textured Ag (1 1 1) films. Incorporation of B facilitates the formation of Ag (1 1 1) coherent twin boundaries, which gives rise to unique nano-tentacle structures. The Ag-B catalyst achieves a faradaic efficiency of CO production of 97.9% at −0.9 V vs RHE with a partial current density that is four times higher compared to pristine Ag. Thus, the inclusion of B into Ag offers a facile approach for circumventing the linear scaling relations, allowing for the design of electrocatalysts with high faradaic efficiencies and current densities.

1. Introduction

The ever-increasing atmospheric concentrations of carbon dioxide (CO_2) poses a formidable threat to modern society due to the severe effects on the climate. Development and utilization of carbon neutral renewable energy technologies is necessary to reduce our dependency on fossil fuels. One such technology is the electrochemical reduction of CO_2, which can directly tackle the CO_2 emission while acting as a potent energy storage method when combined with intermittent renewable energy sources based on e.g., wind and solar power. However, the electrochemical reduction of CO_2 requires the use of stable catalysts that offer high selectivity for a given reaction product. Achieving such a high selectivity while maintaining good reaction rates and low overpotentials remains a challenge due to the slow kinetics of the CO_2 reduction reaction at standard conditions as well as the presence of the competing hydrogen evolution reaction (HER).

One desirable reaction product of CO_2 reduction is carbon monoxide (CO), which is attractive because CO can be used as a feedstock in the Fischer-Tropsch process to produce hydrocarbons. Both Au and Ag catalysts offer high faradaic efficiencies (FE) in the generation of CO due to low inherent binding strength of *CO, which permits an efficient desorption of the molecule from the catalyst surface [1]. While Ag would be the preferred choice due to its significantly lower cost, it requires considerably higher overpotentials than Au to reach high FE(CO). Theoretical studies have indicated that the overpotential is directly linked to the binding energy of the *COOH intermediate, and that increasing the binding energy effectively reduces the overpotential [2]. However, the linear scaling relations of the chemisorption energies between *CO and *COOH makes it difficult to individually tune their binding energies. Meaning that increasing the binding strength of *COOH also increases that of *CO, which may impair its desorption and lead to a reduction in FE. To circumvent these linear scaling relations there needs to be a decoupling between the d-band center and the binding energies of the *COOH and *CO intermediates [3]. Implantation of p-block elements into Ag has emerged as a viable strategy to achieve this decoupling effect [4–6]. Of the p-block elements, Boron (B) has been widely utilized as a dopant in transition metals to produce stable catalysts with enhanced performance toward CO_2 reduction [7,8]. Recent work has also achieved a high uptake of B in Ag [9], with concentrations of 15 at%, showing good compatibility between the materials.

In this study, B was evaluated as a p-block element modifier in Ag through a combination of simulations and experiments. The simulations suggested that B could enhance the formation of CO by lowering the activation barrier of *COOH formation while weakening the binding

* Corresponding author.
E-mail address: kaiying.wang@usn.no (K. Wang).

https://doi.org/10.1016/j.elecom.2023.107600
Received 18 September 2023; Received in revised form 12 October 2023; Accepted 13 October 2023
Available online 14 October 2023

strength of *CO to facilitate rapid desorption from the Ag surface. The methodology developed for synthesizing Ag-B catalysts in this study shows that the incorporation of B in Ag through a magnetron co-sputtering process induces growth of highly textured Ag (1 1 1) films that exhibit 97.9% FE for the electrochemical reduction of CO_2 to CO. This is accompanied by a four-fold increase in the partial current density compared to pristine Ag. The unique nature of the co-sputtering process enables good control of the B content within the Ag films. Structural characterization reveals that the introduction of B into the crystal lattice of Ag induces twin boundary growth and gives rise to unique nano-tentacle structures. The significant improvement in catalytic activity is attributed to a combined contribution of Ag (1 1 1) twin boundaries and incorporation of B, which lowers the activation barrier for *COOH formation.

2. Methods

2.1. DFT simulations

To investigate the effect of B heteroatoms and twin boundaries on the electrochemical CO_2 reduction mechanisms of Ag, an Ag (1 1 1), Ag-B (1 1 1) and TB-Ag slabs were built. DFT calculations of these slabs were computed by using a generalized gradient approximation (GGA) of exchange-correlation functional in the Perdew, Burke, and Ernzerhof (PBE). A plane-wave energy cut off of 400 eV was used together with norm-conserving pseudopotentials, and the Brillouin zone was sampled with a $2 \times 2 \times 1$ Monkhorst–Pack grid. The structure was fully optimized until the force on each atom was less than 10^{-3} eV/Å. To avoid periodic interaction, a vacuum layer of 30 Å was incorporated into the slabs. The free energy (ΔG) was computed from:

$$\Delta G = \Delta E + ZPE - T\Delta S \quad (1)$$

where ΔE was the total energy, *ZPE* was the zero-point energy, the entropy (ΔS) of each adsorbed state were yielded from DFT calculation, and ΔU was applied potential, whereas the thermodynamic corrections for gas molecules were taken from standard tables.

2.2. Catalyst synthesis

4″ wafers of soda-lime glass were diced into 2.5×0.5 cm^2 pieces using a dicing saw (Disco DAD 3220). These samples were cleaned ultrasonically for 10 min in acetone using an ultrasonic cleaner before being rinsed in isopropanol. Next, the samples were loaded into a plasma cleaner, where they were subjected to 10 min of oxygen plasma at a power of 300 W with an Ar flow rate of 50 sccm and an O_2 flow rate of 100 sccm at 58 Pa. The samples were then loaded into the sputtering chamber that also contained an e-beam evaporation unit. First a 15 nm Cr layer was deposited using e-beam (current of 10–15 mA). Then, Ag was deposited using a DC power of 100 W while simultaneously depositing B with an RF power of 0–150 W at room temperature. The resulting films were approximately 1.7 μm thick.

2.3. Material characterization

Low angle XRD (Thermo Fisher Equinox 1000) equipped with a Cu-Kα radiation source with a wavelength of 1.54 Å were used to obtain the XRD spectra. The surface morphology of the samples was investigated by FE-SEM (Hitachi SU 8230). XPS measurements and ion beam milling were performed using a Thermo Fisher ESCALAB 250Xi using a monochromatic Al X-ray source. Ion milling was performed using Ar ion energies of 0.5 and 2 keV. The TEM and STEM images were obtained at 200 kV using a FEI Titan Themis 200 TEM. The AFM measurements were conducted with a Park Systems XE-200 AFM in non-contact mode using an ACTA-200Si probe with a tip radius of <10 nm.

2.4. Electrochemical measurements

The electrochemical measurements were conducted with a CHI660E electrochemical workstation in a custom-made H-cell made of glass (Adams and Schittenden). A Nafion 117 proton exchange membrane separated the anodic and cathodic compartment, which were both filled with 75 mL of 0.5 M $KHCO_3$ electrolyte saturated with CO_2 (pH of 7.4). iR compensation was performed before each measurement by monitoring the resistance vs. the open circuit potential. All electrochemical measurements were performed in a three-electrode configuration using a Pt wire counter electrode and an Ag/AgCl (3 M KCl) reference electrode. The catalysts were tested at each potential for 20 min and fresh electrolyte was used for every catalyst. All catalysts were tested three times. Subsequently, all potentials were converted to the RHE scale using the Nernst equation:

$$E\ vs\ RHE = E\ vs\ Ag/AgCl(3MKCl) + 0.209V + 0.05916 \times pH \quad (2)$$

2.5. Product analysis and quantification

The gaseous reaction products were quantified using a Shimadzu-GC-2010 PLUS gas chromatograph (GC) equipped with a ShinCarbonST column and a dielectric-barrier discharge ionization detector (BID). The gas was sampled every 20 min with the setup connected in an on-line configuration [10]. The Faradaic efficiency (FE) was calculated using the formula in equation (3), where m is the number of moles of product derived from the GC measurement, n_x is the number of electrons required for reduction to product ×,F is Faraday's constant (96500C/mol), and Q is charge (C). In our case the charge was calculated as the time it takes to fill the sample loop multiplied by the current.

$$FE = \frac{m^* n_x^* F}{Q} * 100 \quad (3)$$

3. Results and discussion

DFT simulations were performed to determine the effect of B on the catalytic performance of Ag. The Ag (1 1 1) surface was used in the simulations, with B placed interstitially into the lattice according to figure S1. An upshift in the d-band center (ε_d) towards the fermi level (E_f) of 0.24 eV is observed for the partial density of states (PDOS) with the addition of B (Fig. 1a-c). According to the d-band center theory, the bonding strength of an adsorbate to a transition metal surface is dictated by the filling of the bonding and antibonding states. Shifting of the d-band towards the fermi level (E_f) is accompanied by emptying of the antibonding states as they are forced above E_f. Therefore, the d-band center can rather accurately predict the bonding strength and interaction of an adsorbate at a transition metal surface, where a ε_d that is close to the E_f, exhibits a stronger reactivity. Therefore, in the case of Ag, where the antibonding states are always filled, a stronger chemisorption can occur by reducing the filling of the antibonding states. Thus, the observed upshift should cause a stronger reactivity for Ag-B relative to the pristine Ag (1 1 1) surface. Next, we calculated the free energy profile for the two surfaces (Fig. 1d). In both slabs, the formation of *COOH is the rate determining step (RDS), but the B-doped Ag surface exhibits an activation barrier (E_a) of 1.33 eV, that is 0.25 eV lower than the pristine Ag (1 1 1) surface due to strengthening the *COOH binding. Thus, the stronger binding of *COOH to the Ag-B surface is in line with the observed shift in ε_d. Interestingly, *CO binds weaker to the Ag-B surface than the pristine Ag (1 1 1) by ~0.15 eV. A more rapid desorption of *CO is thus expected for the Ag-B catalyst. The destabilization of the *CO intermediate is interesting as it cannot be explained by the shift in the d-band center. However, the preferential stabilization of *COOH over *CO is consistent with the trend observed in high-throughput screening of p-block dopants in Ag [6]. The phenomenon has been attributed to a covalency-aided electrochemical reaction (CAER) mechanism, which

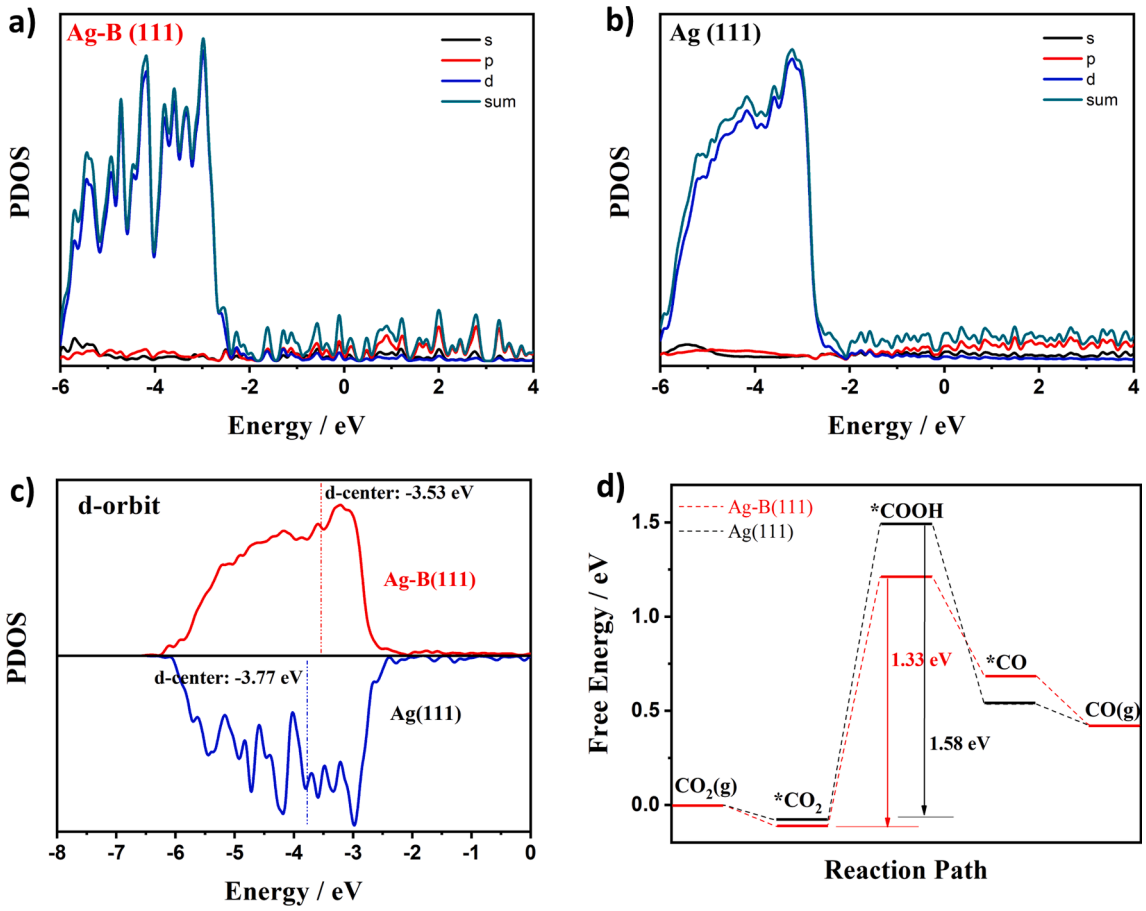

Fig. 1. Theoretical simulations for the B-doped Ag (1 1 1). PDOS for (a) Ag-B and (b) Ag (1 1 1), and (c) comparison of the d-band of the two structures. (d) Free energy diagram for Ag-B and Ag (1 1 1).

arise due to a difference in the σ-binding mechanisms between the COOH and CO intermediates. More precisely, the CO intermediate requires additional energy to form a covalent bond since it first needs to empty the p_z orbital of the dopant site. Based on the DFT simulations we determined that B was promising candidate for enhancing the electrocatalytic performance of Ag, and therefore proceeded to synthesize B-modified Ag catalysts.

Thin film catalysts (~1.7 μm film thickness) were synthesized through a co deposition of Ag and B by magnetron sputtering as depicted in Fig. 2a. The B concentration was controlled by adjusting the RF power of the B target while keeping the DC power of the Ag target constant. Films with three different concentrations of B were made. These were labelled based on the RF power used for the B deposition as Ag (0 W), Ag-B-1 (100 W), and Ag-B-2 (150 W). The structural properties of the films were investigated by X-ray diffraction (XRD), with the respective patterns seen in Fig. 2b. The pristine Ag film displayed a polycrystalline FCC crystal structure, commonly obtained through magnetron sputtering deposition of metal films. However, the co-sputtering of B induced a significant increase in Ag (1 1 1) peak intensity while simultaneously reducing the intensity of other peaks. The Ag (1 1 1) peak intensified with increased B concentration and becomes totally dominant for the Ag-B-2 film. There were no peaks associated with the AgB_2 phase, which tend to be prevalent at ~28° [11]. Furthermore, it was observed that the Ag (1 1 1) peak shifts to lower angles (Fig. 2c) with increasing concentrations of B, suggesting that B causes an expansion of the lattice. To understand the transformation in crystal structure, a set of scanning transmission electron microscopies (STEM) and high-resolution transmission microscopy (HRTEM) were performed on the Ag-B-2 film (Fig. 2d). The cross-sectional images show densely stacked columnar grains aligned in the growth direction. HRTEM performed on these columns reveals a high density of 5–10 nm wide Ag (1 1 1) coherent twin boundaries (TB) aligned perpendicular to the growth direction. The lattice spacing is measured to be 2.385 Å, which is larger than the expected value for Ag (1 1 1) of ~2.360 Å. The selected area electron diffraction (SAED) shows a spotted pattern, which is indicative of a single crystal structure. Additionally, the pattern consists of duplicate points, which is a characteristic of twinned crystals [12]. Thus, the co-deposition of B facilitates Ag (1 1 1) TB growth, whose numbers increase with increasing B concentration, and is visible by a dominant Ag (1 1 1) peak in the XRD spectra. Growth of TB's is highly related to the stacking fault energy (SFE) [13], where metals exhibiting a low SFE tend to form TBs more easily. While Ag is one of the FCC metals with the lowest SFE, the formation of TBs through sputter deposition is usually only observed for epitaxially grown Ag [14]. In contrast, by adding metals and in some cases non-metals to Ag in low concentrations [15], a further reduction in the SFE can be achieved. It is therefore likely that B reduced the SFE of Ag, which favored the observed formation of TB's.

The surface morphology of the films can be seen in Fig. 2e. A granular structure, with ~100 nm wide grains is observed for the pristine Ag film. Introduction of boron gives rise to tentacle structures, with each tentacle being approximately 30–50 nm wide and 100–200 nm long. A mixture of tentacles and grains is attained for the Ag-B-1 film, whereby a full transition into tentacle structures is observed for the Ag-B-2 film. Atomic force microscopy (AFM) was used to gain information about the surface topography. The AFM images display a film morphology that is identical to the SEM images (figure S2) and shows an increase in roughness when B is introduced into the films, from ~7.2 nm for the Ag film to 12.0 nm for Ag-B-2 film. However, there is only a minor

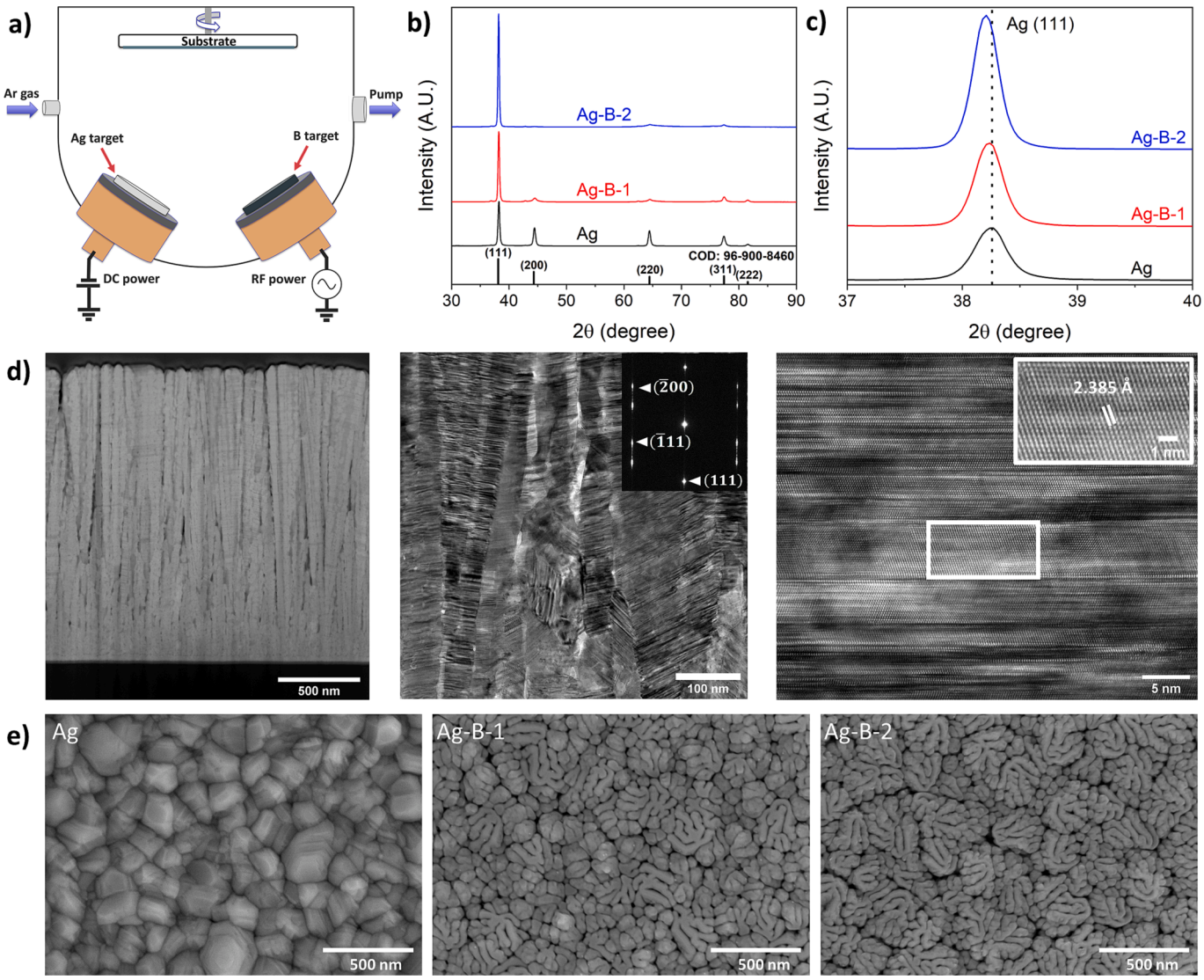

Fig. 2. Synthesis and structural characterization of the Ag-B films. (a) Schematic of the sputtering setup. (b)-(c) XRD spectra of the films. (d) STEM and HRTEM of the Ag-B-2 sample. (e) SEM images of the films.

difference in roughness between the Ag-B-1 and Ag-B-2 films (<1 nm).

X-ray photoelectron spectroscopy (XPS) and Auger electron spectroscopy (AES) were performed to gain insight into the chemical structure of the films. The XPS spectra display strong peaks for Ag3d (Fig. 3a), and the B1s peak is found at ~188 eV for Ag-B-1 and Ag-B-2 (Fig. 3b). According to the XPS data, the atomic ratio of B/Ag was 7 at% for Ag-B-1 and 19 at% for Ag-B-2. While a positive peak shift of ~0.2 eV is detected for the Ag-B films relative to the pristine Ag film (Fig. 3c), the shift correlates with the difference in oxygen concentration at the surface, which was found to be 38.3, 14.6, and 25.2 at% for the Ag, Ag-B-1, and Ag-B-2 samples, respectively. Attempts at removing approximately 200 nm of the top surface layers by ion milling prior to the XPS measurements yielded no B1s peak for any of the samples. AES performed on two different points of the Ag-B-2 film gave a B to Ag concentration of 28 and 25 at% (Fig. 3d), which is higher than that obtained from the XPS. These values were reduced to 12 and 0 at% respectively following ion milling of the samples for 6 s and 18 s prior to the measurement (figure S3). Due to the nature of the co-sputtering process used to synthesize the films, it is expected that B is evenly distributed throughout the material. Thus, it is highly unlikely that the B is primarily located near the top surface, which could be interpreted from the XPS and AES measurements following the ion milling. Instead, a difference in the sputtering yield for the elements could explain the disappearance of B after ion milling. This could further be exacerbated due to the existence of TB's, which can strengthen the mechanical properties of Ag, and potentially reduce its sputtering yield further. In fact, the preferential removal of B from ion milling has previously been observed for various transition metal borides, where increasing the Ar^+ energy was shown to promote this effect [16]. However, reducing the Ar^+ energy of the ion beam from 2 keV to 0.5 eV did not make any noticeable changes, and the B1s peak remained undetectable.

The catalytic performance of the catalysts towards the electrochemical CO_2 reduction was evaluated in an H-cell, with all potentials referenced to a reversible hydrogen electrode (RHE). The tests were conducted in the potential range from −0.6 to −1.0 V, where the analysis of the gaseous reaction products showed that the catalysts mainly produced CO and H_2. The FE(CO) obtained at each potential can be seen in Fig. 4a. The pristine Ag catalyst displays a gradual increase in FE(CO) as the potential increases, reaching a peak FE (CO) of 86.5% at −1.0 V. In the potential range of −0.6 V to −0.7 V the FE(CO) is below 30% for Ag, but nearly doubles as the potential reaches −0.8 V. The Ag-B-1 catalyst show a similar behavior, but generally exhibit higher FE(CO) than Ag. On the other hand, the Ag-B-2 catalyst shows much higher selectivity towards CO at lower overpotentials, with four times the FE

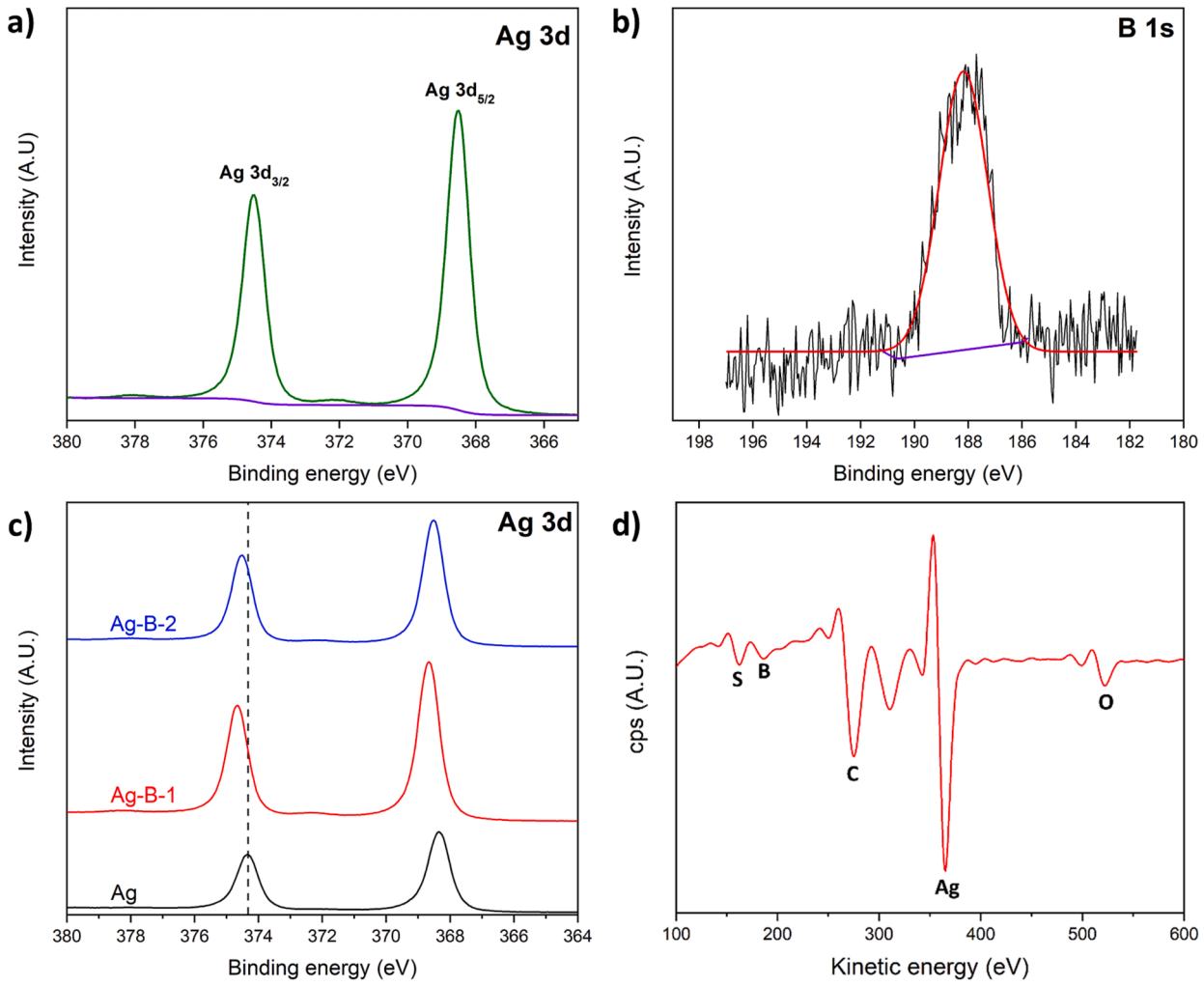

Fig. 3. Characterization of the chemical properties of the films. XPS spectra obtained from the Ag-B-2 sample with (a) Ag3d and (b) B1s. (c) Ag3d XPS spectra of the films. (d) AES spectrum of the Ag-2-B sample.

(CO) of Ag at −0.6 V, while achieving a FE(CO) of ~79% at −0.7 V. Moreover, the FE(CO) reaches 97.9% at −0.9 V, considerably higher compared to Ag, which attains 79% at the same potential. Fig. 4b shows the CO partial current density (J_{CO}) for the catalysts, where an increase in J_{CO} can be seen the Ag-B catalysts. A substantial increase in J_{CO} is seen for Ag-B-2 at all potentials compared to the Ag catalyst. At −0.9 V the Ag-B-2 catalyst exhibits a J_{CO} of −5.6 mA/cm^2, more than 4 times that of the Ag catalyst (−1.3 mA/cm^2). Next, we tested the stability of the Ag-B-2 catalyst by extending the reaction period to ten hours at a potential of −0.9 V. The FE(CO) and current density were plotted as a function of time (Fig. 4c), showing a FE(CO) close to 98% for the first six hours, whereas a slight decline and instability is observed, but the FE(CO) remains above 90% for the entirety of the test. Similarly, a slight decrease in current density is observed over time, but this can be explained by water evaporation due to the continuous flow of CO_2, which reduced the liquid level in the glass cell and hence the effective surface area of the catalyst that was in contact with the solution.

Since the increase in B concentration is accompanied by a change in morphology and crystal structure, it makes it hard to pinpoint the main contributing factor to the observed enhancement in catalytic activity. However, based on previous studies on single crystals, Ag (1 1 1) should exhibit the largest activation barrier (E_a) for *COOH formation compared to Ag (1 0 0) and Ag (1 1 0) [17]. Therefore, we reason that the presence of Ag (1 1 1) is not responsible for the observed improvement. However, the Ag-B-2 catalyst show a significant number of coherent twin boundaries, which have been identified as important active sites for CO_2 reduction for both Cu and Ag [12,18]. We therefore employed DFT simulations to determine the effect of these TB's using a model consisting of a single coherent Ag (1 1 1) TB (figure S4). The free energy profile (Fig. S4b) shows that the formation of *COOH remains the RDS, but the E_a is decreased from 1.58 eV to 1.37 eV for TB-Ag. While *COOH exhibits a stronger binding on TB-Ag (1.094 eV) than Ag-B (1.216 eV), the E_a for *COOH formation is slightly higher on TB-Ag by 0.04 eV due to strengthening the binding of $*CO_2$. Furthermore, the desorption of *CO does not readily occur for TB-Ag as *CO binds stronger on TB-Ag than on the pristine Ag (1 1 1) surface by ~0.27 eV, making the desorption of *CO have a barrier of 0.16 eV. In general, all the intermediates bind stronger to the TB-Ag surface compared to the pristine Ag (1 1 1), displaying dependence of the linear scaling relations. From these findings the TBs should be beneficial for the electrochemical CO_2 reduction to CO. Therefore, considering the collective contribution of B and TB's, it is reasonable to assume that the activation barrier for *COOH formation will be reduced for the Ag-B-2 catalyst, since both the TB's and the incorporation of B strengthens the binding of *COOH. On the other hand, *CO binds stronger on TB-Ag and weaker on Ag-B relative to the pristine Ag (1 1 1), which could suggest that their combined contribution could leave the binding strength of *CO relatively unaffected. Additionally, the catalyst benefits from the enhanced adsorption of CO_2 observed on the TB's. Thus, introduction of B into the Ag effectively allows for strengthening the binding energy of the *COOH

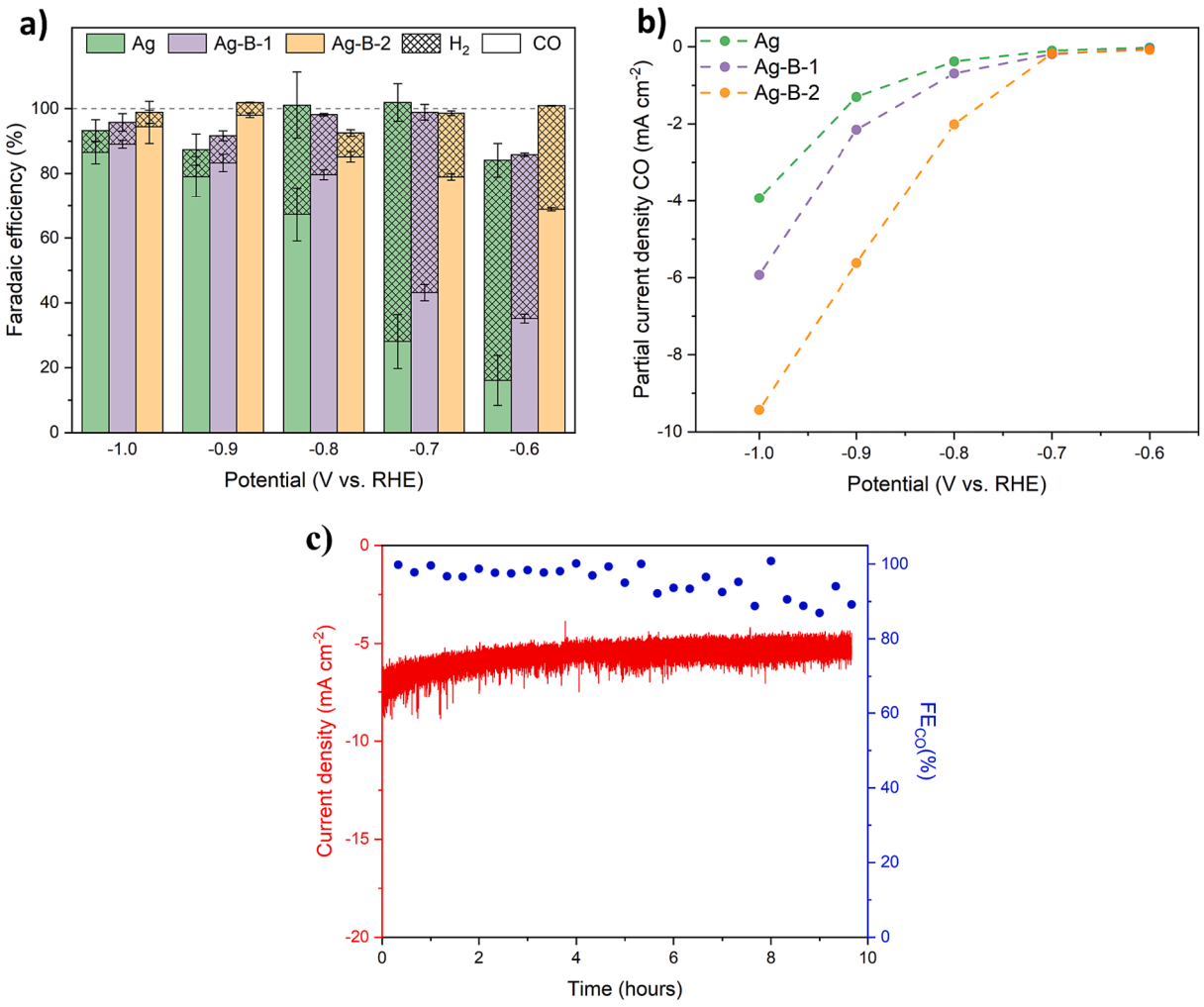

Fig. 4. Electrochemical characterization of the Ag-B catalysts. (a) Faradaic efficiency as a function of applied potential. (b) CO partial current density, and (c) stability test conducted at −0.9 V vs. RHE for the Ag-B-2 catalyst.

intermediate independent of *CO and thereby circumventing the scaling relations.

4. Conclusion

In summary, we have investigated the use of B as a modifier in Ag for the purpose of enhancing the electrochemical reduction of CO_2 to CO. Theoretical simulations show that the introduction of B into the Ag lattice can lower the activation barrier for *COOH formation while simultaneously reducing the binding strength of *CO to allow for rapid desorption. Thin film Ag-B catalysts were synthesized through a magnetron co-sputtering process, where the incorporation of B facilitated the growth of coherent Ag (1 1 1) twin boundaries due to lowering the SFE, leading to highly textured Ag (1 1 1) films. The surface morphology, as revealed by SEM, undergoes drastic changes when increasing the B concentration, from granular to unique nano-tentacles structures. These Ag-B catalysts exhibit considerably improved catalytic properties for electrochemical CO_2 reduction, with a faradaic efficiency of 97.9% for CO at −0.9 V vs. RHE. The unique ability to increase the binding strength of *COOH while destabilizing *CO offers a potent strategy for the development of highly selective catalysts for the electrochemical reduction of CO_2.

CRediT authorship contribution statement

Kim Robert Gustavsen: Conceptualization, Methodology, Investigation, Visualization, Writing – original draft. **Hao Huang:** Methodology, Software, Visualization. **Erik Andrew Johannessen:** Supervision, Writing – review & editing. **Kaiying Wang:** Supervision, Funding acquisition, Writing – review & editing.

Declaration of Competing Interest

The authors declare that they have no known competing financial interests or personal relationships that could have appeared to influence the work reported in this paper.

Data availability

Data will be made available on request.

Acknowledgements

The authors K.R.G. and K.W. acknowledge the research grants from EEA (European Economic Area)-Norway-Romania project #Graftid, RO-NO-2019-0616 and EEA-Poland-NOR/POLNORCCS/ PhotoRed/0007/2019-00. K.R.G acknowledge support from the Norwegian Micro- and Nano- Fabrication Facility (NorFab, No. 245963/F50) and the strategic research plan of the University of South-Eastern Norway. The author H. H. acknowledges Marie Skłodowska-Curie Actions individual fellowship CarbonChem 101024758.

Appendix A. Supplementary data

Supplementary data to this article can be found online at https://doi.org/10.1016/j.elecom.2023.107600.

References

[1] A. Bagger, W. Ju, A.S. Varela, P. Strasser, J. Rossmeisl, Electrochemical CO2 Reduction: A Classification Problem, ChemPhysChem 18 (2017) 3266–3273.

[2] Y. Zhang, L. Liu, L. Shi, T. Yang, D. Niu, S. Hu, X. Zhang, Enhancing CO2 electroreduction on nanoporous silver electrode in the presence of halides, Electrochim. Acta 313 (2019) 561–569.

[3] F. Calle-Vallejo, D. Loffreda, M.T.M. Koper, P. Sautet, Introducing structural sensitivity into adsorption–energy scaling relations by means of coordination numbers, Nat. Chem. 7 (2015) 403–410.

[4] S. Liu, H. Tao, Q. Liu, Z. Xu, Q. Liu, J.-L. Luo, Rational Design of Silver Sulfide Nanowires for Efficient CO2 Electroreduction in Ionic Liquid, ACS Catal. 8 (2018) 1469–1475.

[5] J. Gao, C. Zhu, M. Zhu, Y. Fu, H. Huang, Y. Liu, Z. Kang, Highly Selective and Efficient Electroreduction of Carbon Dioxide to Carbon Monoxide with Phosphate Silver-Derived Coral-like Silver, ACS Sustain. Chem. Eng. 7 (2019) 3536–3543.

[6] H.-K. Lim, H. Shin, W.A. Goddard, Y.J. Hwang, B.K. Min, H. Kim, Embedding Covalency into Metal Catalysts for Efficient Electrochemical Conversion of CO2, J. Am. Chem. Soc. 136 (2014) 11355–11361.

[7] Y. Zhou, F. Che, M. Liu, C. Zou, Z. Liang, P. De Luna, H. Yuan, J. Li, Z. Wang, H. Xie, H. Li, P. Chen, E. Bladt, R. Quintero-Bermudez, T.-K. Sham, S. Bals, J. Hofkens, D. Sinton, G. Chen, E.H. Sargent, Dopant-induced electron localization drives CO2 reduction to C2 hydrocarbons, Nat. Chem. 10 (2018) 974–980.

[8] C. Chen, X. Sun, L. Lu, D. Yang, J. Ma, Q. Zhu, Q. Qian, B. Han, Efficient electroreduction of CO2 to C2 products over B-doped oxide-derived copper, Green Chem. 20 (2018) 4579–4583.

[9] Y. Li, H. Yu, Z. Wang, S. Liu, Y. Xu, X. Li, L. Wang, H. Wang, Boron-doped silver nanosponges with enhanced performance towards electrocatalytic nitrogen reduction to ammonia, Chem. Commun. 55 (2019) 14745–14748.

[10] K.R. Gustavsen, E.A. Johannessen, K. Wang, Sodium Persulfate Pre-treatment of Copper Foils Enabling Homogenous Growth of Cu(OH)2 Nanoneedle Films for Electrochemical CO2 Reduction, ChemistryOpen 11 (2022) e202200133.

[11] J. Pelleg, M. Rotman, M. Sinder, Borides of Ag and Au prepared by magnetron sputtering, Physica C 466 (2007) 61–64.

[12] C. Tang, P. Gong, T. Xiao, Z. Sun, Direct electrosynthesis of 52% concentrated CO on silver's twin boundary, Nat. Commun. 12 (2021) 2139.

[13] D.C. Bufford, Y.M. Wang, Y. Liu, L. Lu, Synthesis and microstructure of electrodeposited and sputtered nanotwinned face-centered-cubic metals, MRS Bull. 41 (2016) 286–291.

[14] D. Bufford, H. Wang, X. Zhang, High strength, epitaxial nanotwinned Ag films, Acta Mater. 59 (2011) 93–101.

[15] L. Velasco, A.M. Hodge, The mobility of growth twins synthesized by sputtering: Tailoring the twin thickness, Acta Mater. 109 (2016) 142–150.

[16] G. Greczynski, L. Hultman, Towards reliable X-ray photoelectron spectroscopy: Sputter-damage effects in transition metal borides, carbides, nitrides, and oxides, Appl. Surf. Sci. 542 (2021), 148599.

[17] E.L. Clark, S. Ringe, M. Tang, A. Walton, C. Hahn, T.F. Jaramillo, K. Chan, A. T. Bell, Influence of Atomic Surface Structure on the Activity of Ag for the Electrochemical Reduction of CO2 to CO, ACS Catal. 9 (2019) 4006–4014.

[18] C. Tang, J. Shi, X. Bai, A. Hu, N. Xuan, Y. Yue, T. Ye, B. Liu, P. Li, P. Zhuang, J. Shen, Y. Liu, Z. Sun, CO2 Reduction on Copper's Twin Boundary, ACS Catal. 10 (2020) 2026–2032.